Effects of ion adsorption on graphene oxide films and interfacial water structure: A molecular-scale description

Amanda J. Carr [a], Raju R. Kumal [a], Wei Bu [b], Ahmet Uysal [a, *]

[a] *Chemical Sciences and Engineering Division, Argonne National Laboratory, Lemont, IL, 60439, United States*
[b] *NSF's ChemMatCARS, The University of Chicago, Chicago, IL, 60637, United States*

ABSTRACT

Graphene oxide is a promising, emerging separation material, as it is durable, dispersible in water, and has naturally forming functional groups. Bulk studies using graphene oxide flakes have demonstrated impressive metal adsorption. However, little interfacial information about water and metal organization near graphene oxide is available. A mechanistic understanding of water and ions interactions with graphene oxide films is critical toward advanced separations, including improved sorption efficiency and membrane regeneration. We study metal ion and local water organization near graphene oxide thin films formed at the air/water interface. These films are not typical membranes and allow us to determine nanoscale information about the graphene oxide-water interface. We accomplish this with x-ray reflectivity (XR), x-ray fluorescence near total reflection (XFNTR), and vibrational sum frequency generation spectroscopy (SFG). These interface-specific techniques provide the electron density profile normal to the interface, number of adsorbed ions, and information about the orientational ordering and hydrogen-bonding network of interfacial water, respectively. Via XFNTR and SFG, we find that trivalent yttrium ions preferentially adsorb to graphene oxide and affect its structure, compared to divalent strontium and monovalent cesium ions. Two different interfacial water populations can be described, based on their hydrogen bonding strength, and the adsorbed ions affect these populations differently. These results provide fundamental information about ion and water organization at the interface and help address the large computational-experimental agreement gap for graphene oxide systems. Additionally, they are relevant for improved soft-scaffold graphene oxide membranes and downstream applications.

© 2022 Published by Elsevier Ltd.

1. Introduction

Graphene oxide (GO), the oxidized analogue of *sp*[2]-hybridized graphene, is a promising, emerging separations material that is well-suited for metal ion adsorption [1]. GO flakes are typically synthesized through chemical exfoliation of graphite [2]. In general, GO flakes have both hydrophilic edges and hydrophobic basal planes [3], meaning they are dispersible in water, durable [4,5], and surface active [6,7]. The final chemical and physical properties of the flakes strongly depend on the synthetic route [8,9] with minor changes affecting average flake size [7,10,11] and polydispersity [4], as well as the number density, placement, and type of oxygen-based functional groups [7,12]. Consequently, adsorption studies using GO-based separation membranes have demonstrated a range of sorption capabilities, likely linked to small changes in GO preparation and final structure [8]. Despite the widespread applicability of GO, there is limited fundamental molecular adsorption information. A molecular-level understanding of interfacial ion adsorption is critical toward developing GO as a useful membrane material, with improvements including increased sorption efficiency and membrane regeneration.

GO as a filtration medium has shown useful results for both gas [13] and liquid applications [14]. In these systems, the diffusive species navigate through micro-channels formed in between dried GO flakes [15,16], the size of which can be successively manipulated via cross-linking flakes with ions and polymers [4,17,18] to affect permeability. Adsorption studies using similar densely-packed GO films have demonstrated permeation and separation success with small monovalent ions [19] and alcohols [20]. Pure GO membranes swell upon addition of water, which can affect filtration by

changing inter-flake spacing and micro-channel sizes [16]. To provide additional structural support, separations with GO composites have been investigated, including cellulose [11], and alginate and chitosan [21], among other polymers [22]. These applied studies report varying sorption success without specifically investigating the molecular-scale details.

Bulk adsorption studies utilizing GO in model aqueous systems have probed the applicability of GO in a range of separation efforts including: cesium [23–25], strontium [23,26,27], technetium [27], lead [28], europium [25,27,29–31], thorium [27,32,33], uranium [25,27,29,31,32,34–36], neptunium [27,32], plutonium [27], and americium [25,27,31]. Few studies have also considered adsorption of other molecules on GO [37] and adsorption of GO on other materials [38,39]. Bulk techniques, namely FTIR, Raman, UV−vis, and x-ray photoelectron spectroscopy (XPS), have identified varied adsorbed metal-GO binding, ranging from likely electrostatics [23,25] to specific binding with sulfur- and oxygen-based groups [25,32,40], although the exact binding mechanisms remain unknown.

Computational efforts have also investigated GO adsorption to understand nanoscale details about the binding mechanisms. Barker et al. reported binding energies between GO flakes and perfluorinated molecules calculated using density functional theory and suggested van der Waals interactions dominate adsorption [41]. Li et al. used first-principles computations of iron on GO flakes to calculate binding strengths as well [42]. Surface complexation modelling has shown some metals adsorb by interacting with carboxyl groups located on the GO flakes [29,31,32,43]. These, among many other computational studies, have provided additional mechanism information. However, there is a large jump between computationally modelled nanometer-sized GO flakes and the typically micron-sized GO samples used in experimental membranes. It is inherently difficult to model large membrane systems directly in most simulations. There are also significant variations in GO flake composition and size between experiments and computational studies, which strongly affect adsorption results. Consequently, a large gap in between quantitative computational and experimental agreement still exists, and basic interfacial experiments are necessary.

The amphiphilic and surface-active nature of GO has spurred some interfacial experiments as well. Langmuir-Blodgett films prepared from GO dispersions successfully spread on aqueous subphases have confirmed surface activity [44–47]. Although GO is not a traditional surfactant [8], it can stabilize water-oil emulsions [7,48] with limited studies considering the oil-water interface specifically [49]. The air-water interface is particularly relevant to separation efforts but can be difficult to isolate from the bulk. Synchrotron x-ray reflectivity (XR) measurements are well-suited for interfacial efforts and can provide the total electron density profile (EDP) perpendicular to the air-water interface. Bonatout et al. probed interfacial GO flakes on plain water, using XR, and found spontaneous bilayer formation at low surface pressures [50].

In a different approach, David et al. used vibrational sum frequency generation (SFG) spectroscopy to examine the GO-water interface formed in between GO films spin-coated on sapphire and plain water [51]. SFG is a second-order, non-linear technique where input visible and IR beams overlap spatially and temporally on a sample surface and generate a new frequency (ω) equal to the sum of the input frequencies, i.e. $\omega_{SFG} = \omega_{vis} + \omega_{IR}$. This process is forbidden in centrosymmetric systems within the electric dipole approximation thus eliminating bulk phase contributions [52–54]. David et al. reported both experimental and computational SFG data and demonstrated clear changes in the hydrogen-bonding network of water for GO samples with different degrees of oxidation, which was further investigated in another computational

work [55]. Neither study considered the effects of ion adsorption on the hydrogen-bonding network nor experimentally measured the soft air-water interface.

In this paper, we examine metal ion adsorption onto GO thin films formed at the air-water interface using XR, x-ray fluorescence near total reflection (XFNTR), and SFG spectroscopy (Fig. 1). These self-formed thin films are not membranes, as they are thin and lack a support substrate. Instead, this system functions as a model GO interface for which we can determine nanoscale information about water and ion organization near a particular GO. Such results are directly applicable to soft-scaffold applications and are essential for bridging the computational-experimental information gap. Our XR measurements reveal the structure of the GO thin films. XFNTR is an interfacial-specific fluorescence technique that determines the quantitative adsorbed metal ion density by collecting x-ray fluorescence signal as a function of momentum transfer Q_z around the interfacial critical angle Q_c. SFG data yield molecular-scale information about the hydrogen-bonding network of water, which is directly affected by ion adsorption. Together, these techniques provide detailed nanoscale information about ion adsorption onto soft-scaffold GO films. We find via XFNTR and SFG that trivalent yttrium ions (Y^{3+}) adsorb more strongly compared to divalent strontium (Sr^{2+}) and monovalent cesium (Cs^{1+}) ions. XR reveals a relatively complex GO structure after yttrium adsorption. Y^{3+} also disrupts the hydrogen-bonding network present, as evidenced from SFG. We speculate yttrium interacts with the varied functional groups present on the hydrophilic edges of the GO flakes, meaning ion adsorption to GO is more complex than simple electrostatic attraction.

2. Experimental

2.1. Materials and sample preparation

All chemicals were purchased from Sigma Aldrich and used as is. We prepared 20 mM and 0.05 mM solutions using cesium (I) chloride (CsCl, ≥99.999% trace metals basis), strontium (II) chloride hexahydrate (SrCl$_2$·6H$_2$O, 99.995% trace metals basis), yttrium (III)
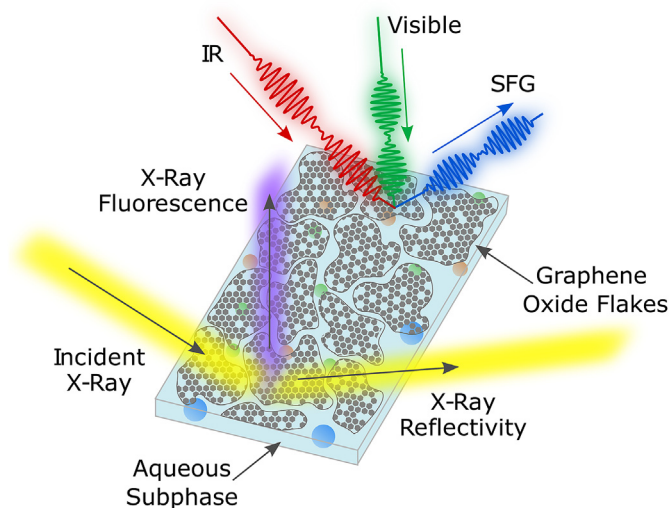

Fig. 1. Experimental cartoon showing interfacial x-ray reflectivity (XR), x-ray fluorescence near total reflection (XFNTR), and vibrational sum frequency generation spectroscopy (SFG) measurements on the air-water interface. GO flakes are pinned on a dilute aqueous subphase. XR measurements provide the total electron density profile perpendicular to the interface. XFNTR yields the quantitative adsorbed ion density. SFG measures changes in the hydrogen-bonding network of water near the interface as induced by metal ion adsorption. (A colour version of this figure can be viewed online.)

chloride hexahydrate (YCl$_3$·6H$_2$O, 99.99% purity), and ultrapure water with a resistivity of 18.2 MΩ cm (Millipore, Synergy Water Purification System). To make the graphene oxide samples, we diluted commercially available graphene oxide (GO, 4–10% edge oxidized, 1 mg/mL, dispersed in water) with 1 part GO and 5 parts methanol (99.8% anhydrous), and sequentially filtered with 1.2, 0.45, and 0.2 μm syringe filters. GO flake size was measured using dynamic light scattering (ZetaSizer Nano ZS).

In general, we prepared films by slowly spreading a small amount of GO from a 1 mL glass Hamilton syringe over the desired aqueous subphase. We monitored the surface pressure with a pressure sensor (Nima) equipped with a chromatography paper Wilhelmy plate. For SFG experiments, monolayers were prepared in a 60 × 20 mm^2 flat-form polytetrafluoroethylene dish via the drop-wise addition of GO until the target surface pressure was obtained. For x-ray experiments and pressure-area isotherms (Supporting Information), films were prepared using a Langmuir trough with a single barrier (Supporting Information). We made Langmuir-Blodgett GO films by preparing a film on a Langmuir trough with two barriers and transferring the film onto clean Si/SiO$_2$ wafers. XPS (Thermo Scientific ESCALAB 250Xi) was completed on Langmuir-Blodgett GO films (Supporting Information).

2.2. Vibrational sum frequency generation spectroscopy experiments

SFG experiments were carried out using an EKSPLA laser system, described in detail elsewhere [56–59]. Briefly, an amplified Nd:YAG laser system produces 29 ps pulses with 28 mJ energy centered at 1064 nm at a repetition rate of 50 Hz. A harmonic unit and a second harmonic crystal split the 1064 nm laser into two beams of 532 nm. One of these 532 nm beams and the 1064 nm beam are used to generate a narrowband IR pulse, tunable from 1000 to 4000 cm^{-1}, via an optical parametric generator and difference frequency generation. The other 532 nm beam is then overlapped spatially and temporally with the narrowband IR pulse at the sample surface to generate the sum frequency signal. A Glan polarizer adjusts the polarization of the final 532 nm beam and SFG signal while computer controlled motorized mirrors adjust the IR beam polarization. A photomultiplier tube connected to a monochromator detects the final SFG signal.

The SFG spectrometer uses a reflection geometry where the incident angles of the 532 nm and IR beams are 60° and 55°, respectively, to the surface normal. We attenuate the visible light to 200 μJ and maintain the IR light at 100 μJ for all measurements. Each spectrum is collected with a 4 cm^{-1} step from 3000 to 3800 cm^{-1}. Each datum point is an average of 300 laser shots. We collect spectra in various polarization combinations and normalize the data to z-cut quartz. The surface pressure for each experiment was 20–22 mN/m and samples were measured at room temperature.

The collected SFG signal (I_{SFG}) is proportional to the product of the incident beams intensities and the square of the effective second order non-linear susceptibility $\chi^{(2)}$ of the interface i.e.

$$I_{SFG} \propto \left| \chi^{(2)} \right|^2 I_{Vis} I_{IR} \tag{1}$$

where

$$\left| \chi^{(2)} \right|^2 \propto \left| \chi_{NR}^{(2)} + \sum_n \frac{A_n}{\omega_{IR} - \omega_n + i\Gamma_n} \right|^2 \tag{2}$$

Here, $\chi_{NR}^{(2)}$ is the non-resonant component of $\chi^{(2)}$, A_n is the

resonant amplitude, ω_n is the resonant frequency, and Γ_n is the dampening constant that determines the peak width, each of the nth vibrational mode while ω_{IR} is the IR beam frequency. For a charged interface, the static electric field allows some bulk contribution to the SFG signal, commonly called the $\chi^{(3)}$ effect [60–62]. For these systems,

$$\left| \chi^{(2)} \right|^2 \propto$$

$$\left| \chi_{NR}^{(2)} + \sum_n \frac{A_n}{\omega_{IR} - \omega_n + i\Gamma_n} e^{i\gamma_n} + \frac{\kappa}{\sqrt{\kappa^2 + \Delta\kappa_z^2}} e^{i\varphi} \chi^{(3)} \Phi_0 \right|^2 \tag{3}$$

where γ is the phase angle of the resonant component of $\chi^{(2)}$, κ is the inverse Debye screening length, $\Delta\kappa_z$ is the inverse SFG coherence length, φ is the $\chi^{(3)}$ phase angle, and Φ_0 is the surface potential. Additional details are provided elsewhere [60].

For the bimodal water region, we fitted SFG data with two Lorentzian peak functions via the sum of least-squares using Equation (3). $\chi_{NR}^{(2)}$ was fitted to plain water data and held constant for other measured concentrations. Peak width and frequency were fitted as global variables for all data sets − only the measured resonance amplitudes for each χ component were fitted individually for each considered concentration.

2.3. Synchrotron x-ray experiments

X-ray experiments were conducted at sector 15-ID-C (NSF's ChemMatCARS) of the Advanced Photon Source at Argonne National Laboratory. We collected XR and XFNTR data using an incident x-ray energy of 18.3 keV. Two motorized slits set the incident beam size to 2 mm horizontally and 0.02 mm vertically. XR signal was detected on a Pilatus 200 K area detector. A Vortex-60EX multi cathode energy dispersive x-ray detector, placed perpendicularly 10 mm above the liquid surface, recorded fluorescence signal. Films were prepared on a Langmuir trough inside a chamber, which was purged with He to reduce background scattering and beam damage.

2.3.1. X-ray reflectivity measurements

We recorded specular x-ray reflectivity as a function of transfer momentum $Q_z = (4\pi /\lambda)\sin(2\theta /2)$ where λ is the wavelength and θ is the incident angle. The sample was shifted periodically to avoid beam damage. Models using different numbers of slabs were used during fitting, as detailed in the Discussion. We fitted the collected XR data to calculated curves using the sum of least-squares via a Parratt formalism to determine slab thickness, roughness, and electron density (Supporting Information). For models with multiple slabs, the roughness values at all interfaces are dominated by surface capillary waves and were consequently forced to be equal [63,64].

2.3.2. X-ray fluorescence near total reflection measurements

The x-ray fluorescence intensities [65] of the $L_{\alpha2}$ (4.287 keV) for Cs, $K_{\alpha1}$ (14.165 keV) for Sr, and $K_{\alpha1}$ (14.958 keV) for Y were collected as a function of Q_z around the critical angle. The beam footprint was always larger than the detector area, meaning only the depth of the illuminated volume varies with incident angle. The total illuminated volume was calculated via the beam dimensions, as described elsewhere [66], and used to calculate XFNTR data via sum of least-squares [66].

3. Results and Discussion

3.1. Y^{3+} adsorption to graphene oxide

We first investigated ion adsorption to GO films spread on high and low concentration YCl_3 subphases, using XFNTR (Fig. 2). This surface-sensitive technique is the most direct way to determine the number of ions adsorbed to the interface. XFNTR measures x-ray fluorescence as a function of momentum transfer Q_z near the critical angle Q_c, which is ~0.0217 $Å^{-1}$ for these systems. Because we do not see interfacial signal for subphases without a GO film, we reasonably posit that metal ions pinned to the interface and detected with XFNTR are adsorbing to the GO. For a 20 mM YCl_3 subphase and a GO film compressed to 20 mN/m, we found 1 adsorbed Y^{3+} per 149 ± 19 $Å^2$. Signal intensity measured at $Q < Q_c$ shows intensity primarily from ions within the interfacial region, as the x-rays undergo total external reflection [63,66,67] and only evanescent waves penetrate a few nanometers of the liquid. Data from this region are highlighted in Fig. 2 inset. Signal intensity at the high Q_z values were larger than predicted by our model. We speculate our GO samples are not smooth monolayers at the air-water interface and instead form crumpled, multilayer structures [50] that can have a non-ideal Y^{3+} ion distribution below the surface. This effect is even more noticeable for GO compressed to 30 mN/m on a 20 mM YCl_3 subphase (Supporting Information).

We next considered dilute YCl_3 subphases to understand adsorption behavior in an unsaturated system. Fig. 3 shows XFNTR data for GO films compressed to 20 mN/m and 30 mN/m spread on 0.05 mM YCl_3. With a lower subphase concentration, we see less bulk signal above Q_c, as the signal from the surface decreases with increasing Q_z, and the bulk concentration is below the limit where their signal can reach to the detector [59,63,68]. The noise in the bulk region data is probably due to a small number of ions with a non-ideal distribution at the interface due to the crumbled GO structure.

We focus on the data below Q_c to understand ion adsorption to the GO. For GO compressed to 20 mN/m, we obtain an ion density of 1 ion per 401 ± 10 $Å^2$ while for GO compressed to 30 mN/m, we find an ion density of 1 ion per 326 ± 6 $Å^2$. The increase in adsorbed ion density for the higher surface compression and overall increase in intensity implies more ions per area are adsorbed to the film. A higher surface pressure compression means more GO is occupying the available film space. Thus, more ions can adsorb and increase

the surface density.

Notably, GO dispersions have varied chemical and physical properties depending on the preparation method, which strongly affects film behavior and subsequent ion adsorption. We are currently investigating these effects in detail, which will be reported in another publication. In this work, we exfoliate commercial GO dispersions with methanol and use filtration to isolate GO flakes. XPS analysis of Langmuir-Blodgett thin film GO samples [7,45] (Supporting Information) provides a rough maximum density estimate of ~1 carboxyl group per 60 $Å^2$ and ~1 epoxy group per 30 $Å^2$. These values represent the higher limit of possible available oxygen groups. Evidently, we observe less adsorbed Y^{3+} than available sites, meaning the theoretical experimental binding capacity for GO is much higher than we observe. In a recent study, we demonstrate enhanced Y^{3+} adsorption onto plain electrified graphene with approximately 1 adsorbed Y^{3+} per 11 $Å^2$ [69]. That system lacked functional groups and demonstrated electrostatic adsorption without disrupting the hydration shell of Y^{3+}. The current GO system demonstrates more complicated adsorption with partial or full dehydration of the adsorbed ions. There is likely a delicate balance between preferential ion interactions with the oxygen functional groups present on the GO film, as previously established in many studies [23,25,32,40], and the energy penalty of partial or full dehydration. We speculate one can tune the degree of functionalization across the graphene-derivative to maximize adsorbed ion loading.

3.2. Interfacial water structure near graphene oxide

We investigated molecular water and ion behavior near GO using SFG, a non-linear interface-specific vibrational technique. We examined the $-OH$ stretch of the water region for our GO films at 20 mN/m on different YCl_3 subphases using SSP (SF, visible, and IR) polarization (Fig. 3A). GO on plain water shows a bimodal peak at maximum intensity with centers at approximately 3200 and 3400 cm^{-1}, assigned to strongly and weakly hydrogen bonded -OH stretches of interfacial water, respectively [70,71]. The absence of signal near 3700 cm^{-1} suggests there are no water molecules with free-dangling -OH bonds pointing upward away from the subphase, meaning a uniform film is present [61,72]. XPS results show primarily carbon and oxygen signal with some sulfur contamination (Supporting Information) [73] and a 5.21 carbon: oxygen ratio, meaning our GO films are primarily carbon and lack a significant
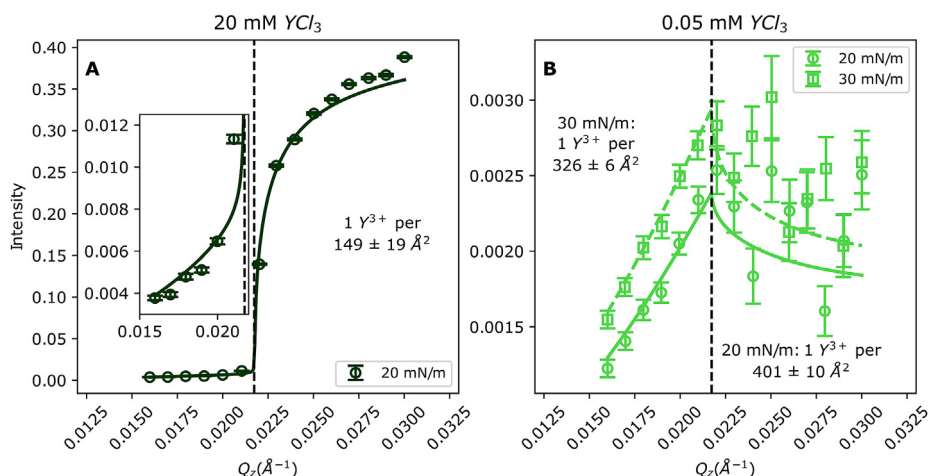

Fig. 2. Surface-sensitive x-ray fluorescence near total reflection (XFNTR) intensity and fits (lines) plotted over inverse momentum Q_z for graphene oxide films spread on 20 mM (A) and 0.05 mM (B) YCl_3. The monolayer was compressed to 20 mN/m for the 20 mM subphase, and to 20 (circles) and 30 (squares) mN/m for the 0.05 mM subphase. Error bars are derived from counting statistics. (A colour version of this figure can be viewed online.)
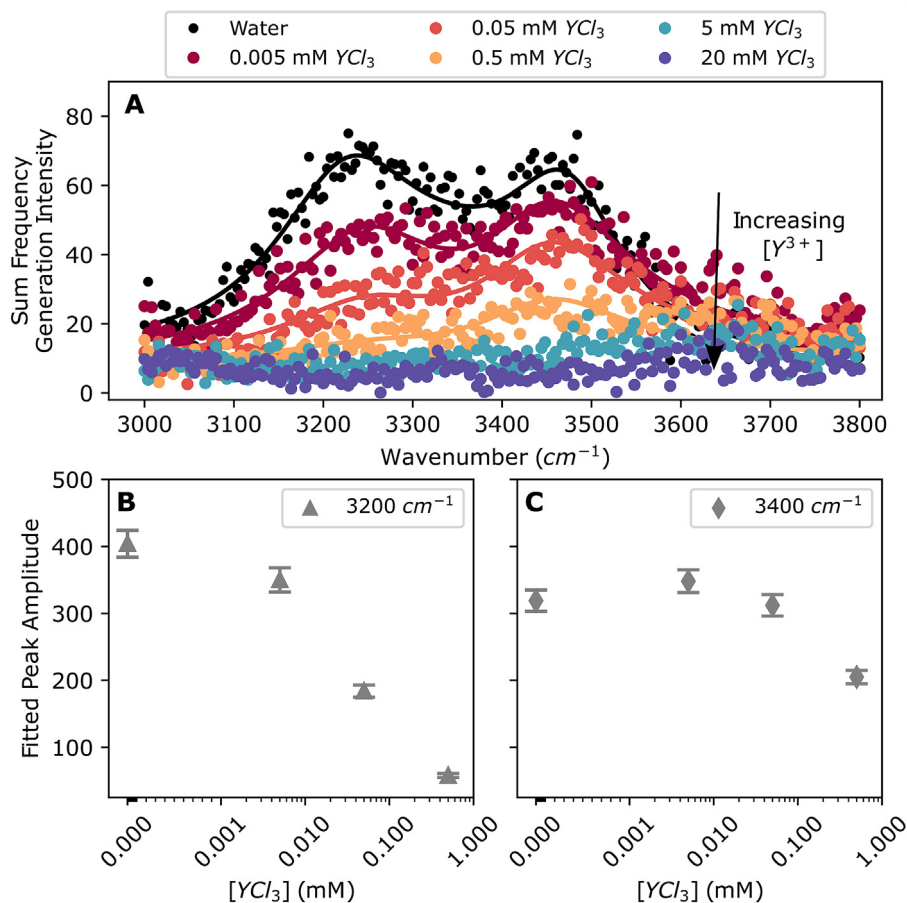
Fig. 3. Sum frequency generation spectroscopy intensity and fits (solid lines) plotted over wavelength for the water region of a graphene oxide film spread over YCl_3 subphases of varying concentration (colors) (A). The surface pressure of the GO was 20 mN/m. Typical water band signal is also shown (black). Fitted $\chi^{(2)}$ peak amplitudes plotted over subphase concentration for the 3200 (B) and 3400 (C) cm^{-1} water signal features. (A colour version of this figure can be viewed online.)

amount of oxygen functional groups. Accordingly, our SFG data agree with other published experimental SFG data on a thermally reduced GO film spin-coated on sapphire [51]. Our GO films are self-assembled at the interface without a solid substrate and can provide adsorption information relevant to soft-scaffold separation systems.

Signal for 0.005 mM YCl_3 shows the water peaks but the absolute intensities are lower. The decrease in intensities can have two main reasons, both resulting from the ion adsorption to the monolayer [56,74,75]. Ion adsorption can screen the surface charge of the interfacial film thus effectively reducing the electric field normal to the liquid surface facing down into the subphase. These screening effects reduce water molecule alignment and decrease SFG signal. This is usually referred to as the $\chi^{(3)}$ effect. Ions can also directly disrupt the orientational ordering of the interfacial water molecules, typically within the first two monolayers of the interface, which directly affects $\chi^{(2)}$. As we continue to increase the subphase concentration, the water peak intensities decrease. Both peaks are completely suppressed for the 5 and 20 mM data, indicating that above a certain ion concentration the interfacial water structure is completely lost. The hydrogen-bonding network of water has been significantly disrupted due to the adsorbed Y^{3+} and no water signal is detected. Hong et al. reported a similar observation using a different GO spread on a NaCl subphase and state the addition of a salt in the subphase decreased SFG intensity by diminishing the $\chi^{(3)}$ effect [76].

Interestingly, the relative water band intensities also change

with increasing subphase concentration. To highlight these changes in water peak intensity as a function of subphase concentration, we fitted the SFG signal to Equation (3), which considers the $\chi^{(3)}$ effect explicitly. The $\chi^{(2)}$ peak amplitudes for the 3200 and 3400 cm^{-1} bands plotted over YCl_3 concentration are presented in Fig. 3B and C. Additional fit parameters are given in Tables S1 and S2. Data were also fitted using Equation (2), without the explicit $\chi^{(3)}$ term, and a similar trend was observed (not shown). Evidently, the fitted amplitude for the 3200 cm^{-1} feature rapidly decreases with increasing YCl_3 concentration while the amplitude of the 3400 cm^{-1} peak remains relatively unchanged. Because we explicitly include $\chi^{(3)}$ within our fitting process, these decreases in amplitude terms are not from changes to the local electric field as induced by shielding from the adsorbed ions. We speculate Y^{3+} adsorption is not simply electrostatic, as features of the hydrogen-bonding network of water change differently. These results reveal a more complicated ion adsorption process that can be overlooked by using bulk experimental techniques. In the absence of metal ions, water can form strong hydrogen bonds with the carboxyl and hydroxyl groups of the GO, which significantly contributes to the 3200 cm^{-1} peak intensity. As metal ions adsorb and disrupt the hydrogen-bonding network of water, we see a large decrease in this peak intensity. We posit the 3400 cm^{-1} band stems from weakly hydrogen bonded water molecules adjacent to the GO or perhaps in between the GO layers, the structure of which will be discussed later. The amplitudes for the 3400 cm^{-1} do not significantly change with subphase concentration, which suggests these weakly

hydrogen bonded water molecules do not change. At concentrations above 5 mM, this band disappears because the adsorbed Y^{3+} have sufficiently disrupted local water organization, and possibly have penetrated the GO layered structure thus affecting any water in between the layers. We present these arguments as first order approximations and are currently investigating water orientation and organization near GO films with molecular dynamic simulations, which can reveal important details [51,68].

3.3. Interfacial graphene oxide structure after Y^{3+} adsorption

Taken together, the XFNTR and SFG analysis show Y^{3+} adsorption onto GO flakes assembled at the air-water interface. XR studies complement these observations by providing the molecular-scale structure of GO films (Fig. 4). XR data collected for GO spread on a dilute 0.05 mM YCl_3 subphase and compressed to 20 mN/m show a small dip around $Q = 0.18$ Å^{-1} and broad peak near $Q = 0.28$ Å^{-1}. The 30 mN/m XR data have a higher intensity overall and show a distinct dip in reflectivity around $Q = 0.16$ Å^{-1} and a larger broad peak around $Q = 0.24$ Å^{-1}. These features imply the film on the liquid surface is not a simple layer in Z-direction and consequently requires a 2-slab model to fit the data and obtain the electron density profile (Fig. 4B). A slab containing a lower electron density was necessary to fit the dips in the XR data. Since the GO electron density is close to the water electron density and capillary oscillations smear the profile, it is difficult to resolve individual flake thickness or number of layers unambiguously. Nevertheless, it is possible to capture the main features of the GO film. We report the variation in fitted electron densities and thicknesses in the Supporting Information.

The resulting electron density profiles are plotted over Z where $Z = 0$ Å is loosely the top of the bulk liquid and Z increases into the air. Both the 20 and 30 mN/m data show an expected increase in density around $Z = -5$ Å, corresponding to the film sitting on a liquid interface, with an enhanced electron density near $Z = -10$ Å. For the 20 mN/m sample, this enhancement has an electron density of 0.52 $e^-/$Å^3 and a thickness of 6.77 Å. The 30 mN/m sample electron density fit gives a slightly higher electron density of 0.54 $e^-/$Å^3 and a slightly smaller thickness of 5.33 Å, also at $Z = -10$ Å. We posit these high electron density slabs represent the interfacial

region closer to the bulk solution that contains adsorbed Y^{3+} and a crumpled, multilayer GO film (Fig. 4C).

Y^{3+} can interact via electrostatics with any available functional groups on the GO. These results can be compared to the bulk GO studies of Am (III) and Eu (III), which have found metal-hydroxyl, -epoxy, and -carboxylate interactions [25]. As Y^{3+} adsorb to the GO, the ions have enough charge to attract deprotonated oxygen-containing and sulfur contaminate groups on the GO. This rearrangement forces the GO flakes to tilt and generates a rough, crumpled GO film that can, in addition to the adsorbed ions, reflect more signal and be detected using XR [48]. Based on the obtained pressure-area isotherms (Supporting Information), the GO film is likely in the same condensed phase at both 20 and 30 mN/m where GO sheets are touching and overlapping to create a multilayer structure [45,47,50]. This means there is little mechanical difference in between the two film structures at these pressures. These structures are also mechanically stable. We observed a similar trend with the XFNTR data where the increase in adsorbed ion density for 20 and 30 mN/m is minimal.

Both profiles also show a lower-density region around $Z = 10$ Å, i.e. closer to air. In the less-compressed 20 mN/m, this region has an electron density of 0.061 $e^-/$Å^3 and a thickness of 16.3 Å. The 30 mN/m sample gives an electron density of 0.030 $e^-/$Å^3 with a larger thickness of 21.4 Å. We linked the roughness of all interfaces, as the interfacial roughness is dominated by capillary waves [63,64], and found a roughness of 4.32 and 4.47 Å for 20 and 30 mN/m, respectively. We speculate this thicker slab represents tilted GO flakes within the crumpled, multilayer GO film (Fig. 4C). A tilt of even a few degrees can increase the effective length of the micron-size GO flakes thus increasing the total layer thickness. The changes in electron density and slab thickness are more pronounced in between the two considered surface pressures. Because these parameters intrinsically covary [77], fits with more similar electron densities and thickness are likely also possible. However, we note that GO is not a typical amphiphilic monolayer and that the overall observed structural differences for 20 and 30 mN/m are minimal.

3.4. Mono- and divalent ion adsorption to graphene oxide

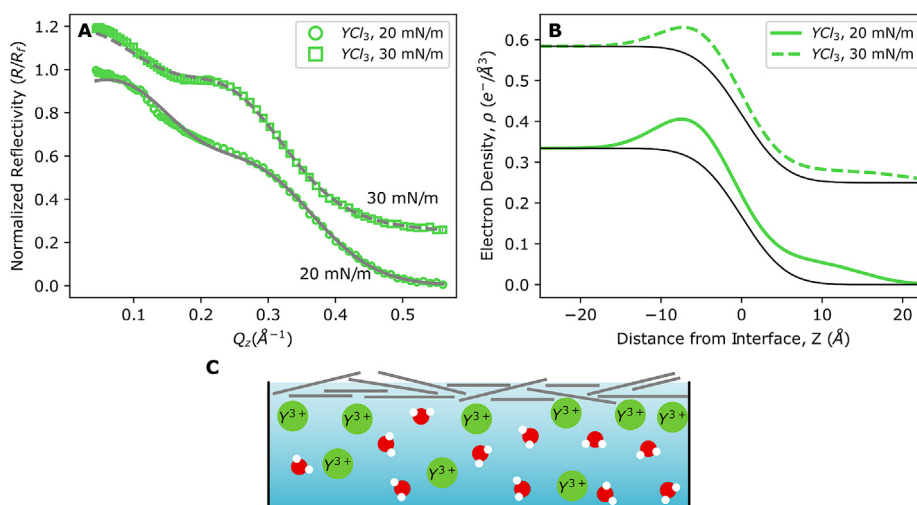As a comparison, we also consider mono- and divalent ion

Fig. 4. Normalized x-ray reflectivity plotted over vertical momentum transfer, Q_z for graphene oxide films compressed to 20 (circles) and 30 (squares) mN/m spread on 0.05 mM YCl_3 subphases (A). Data were fit using a 2-slab model (lines). 30 mN/m data are vertically offset for clarity. Calculated electron density from fitted reflectivity data plotted over distance from interface Z (B) for graphene oxide monolayers compressed to 20 (solid line) and 30 (dashed line) mN/m spread on 0.05 mM YCl_3 subphases. An ideal interface electron density profile is included (black). 30 mN/m data are vertically offset by $+0.25$ $e^-/$Å^3 for clarity. Proposed interfacial structure (not to scale) (C). (A colour version of this figure can be viewed online.)

adsorption to GO films at the air-liquid interface. We measured XFNTR for GO samples spread on high concentration 20 mM CsCl and SrCl$_2$ subphases (Fig. 5A and B). For a GO sample compressed to 20 mN/m, we find 1 adsorbed Cs^{1+} per 345 $\pm$ 73 Å^2 and 1 adsorbed Sr^{2+} per 204 $\pm$ 48 Å^2. XFNTR measured on 0.05 mM CsCl and SrCl$_2$ subphases (not shown) showed no signal, meaning no ions adsorbed within the detection limit, which is typically 1 ion per 50,000 Å^2 [78].

To examine molecular water and ion behavior, we used SFG spectroscopy of the −OH stretch of the water region for GO samples compressed to 20 mN/m and spread over dilute and concentrated subphases (Fig. 5C and D). SFG data for GO on 0.05 mM CsCl are nearly identical to GO on plain water. This means nearly no Cs^{1+} adsorb to the GO, which is consistent with our XFNTR results. The 20 mM CsCl data show an intensity decrease in both water bands, indicative of disruption to the well-ordered hydrogen-bonding network of water near the interface and indirect evidence of ion adsorption. Given the ion adsorption information obtained from the XFNTR analysis, we reasonably posit that for a 20 mM subphase, some Cs^{1+} adsorbs. We see similar behavior for the 20 and 0.05 mM SrCl$_2$ SFG data. In this case, the water peak intensity decreases more for the 20 mM subphase − consistent with a higher adsorbed ion density. Taken together, these XFNTR and SFG data show minimal ion adsorption for both Cs^{1+} and Sr^{2+}. Previous works have demonstrated weak bonding interactions between Cs and bulk GO [23−25] with Cs primarily interacting with hydroxyl, epoxy, and sulfur contaminations [25]. Bulk studies utilizing Sr^{2+} and GO have also found metal interactions with C−O−C and O−C═O, as well as sulfur contaminates [23,26] although the specific adsorption mechanisms are unclear. Evidentially, Y^{3+} adsorbs preferentially to GO compared to both Cs^{1+} and Sr^{2+}. This adsorption result is not surprising given the expansive literature of high valency ion adsorption [43]. However, the structural changes we observe within the GO film after adsorption are novel and directly applicable to downstream application development. Our interfacial, *in situ* techniques reveal considerable film changes in thickness in relevant water and ion conditions.

We analyzed the GO interfacial structure for samples spread on CsCl and SrCl$_2$ subphases using XR (Fig. 6A). For GO spread on 0.05 mM CsCl, the XR data is nearly featureless with little difference in between films compressed to 20 and 30 mN/m. The slight increase in reflectivity for the 30 mN/m sample is consistent with more GO material within the probed interfacial region, which can then reflect more signal. We fit these XR data using 1 slab to generate an electron density profile (Fig. 6B). These XR data lack distinguishable features and the absolute slab thickness and electron density parameters are not perfectly reliable because these parameters intrinsically covary [77]. However, the EDPs generated from combinations of these parameters show little variance.

For a 0.05 mM CsCl subphase, the 20 mN/m data yield an electron density of 0.41 e^-/Å^3, a thickness of 6.8 Å, and a subphase-linked roughness of 4.25 Å while the 30 mN/m data provide electron density of 4.9 e^-/Å^2, a thickness of 14.1 Å, and a subphase-linked roughness of 4.04 Å. We note the resolution of these XR measurements is ~5.6 Å. Given our XFNTR and SFG analysis, we reasonably posit that the XR data show GO flakes assembled at the interface with nearly no adsorbed metal ion interference. The 20 mN/m case then likely shows a layer of partially hydrated GO, consistent with other XR measurements [50], while the 30 mN/m case shows a more crumpled GO structure, as the electron density and thickness both increase. We posit the increase in surface pressure forces the GO flakes to tilt and create a thicker film. Compared to the Y^{3+} XR data, we speculate the Y^{3+} data reveal a complex interfacial structure with both increased electron density and layer thickness due to the adsorbed ions. These Y^{3+} ions disrupt clear layering, as also observed by others using neat water [50], and create a complicated multilayer structure containing GO flakes, adsorbed Y^{3+}, and water.

To understand the GO structure in a partial adsorption case, we measured XR for GO on 20 mM SrCl$_2$ (Fig. 6A). Interestingly, the XR data are again nearly featureless except for the small increase in electron density for the 30 mN/m data, consistent with more
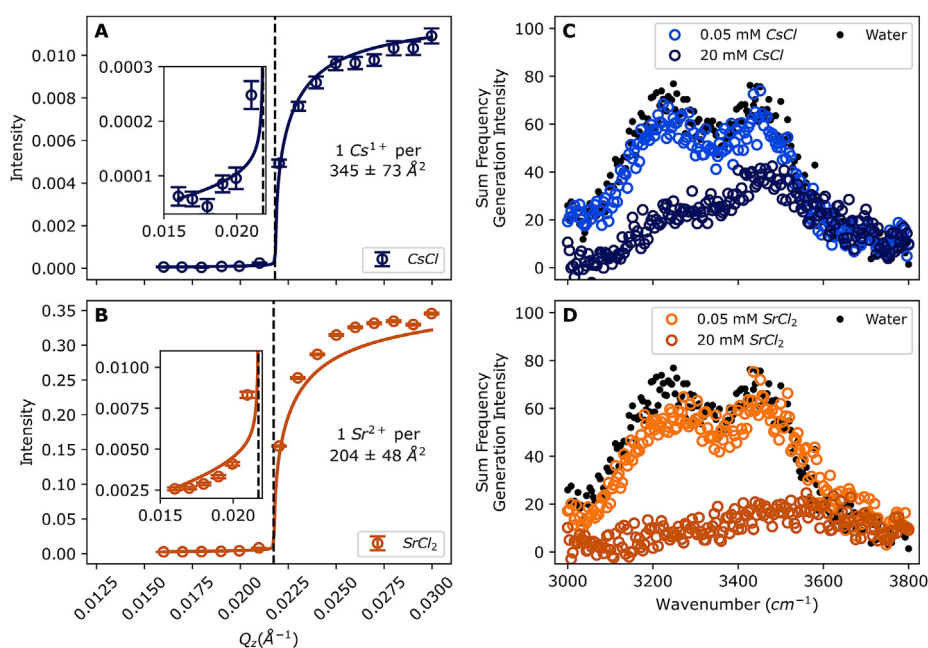

Fig. 5. Surface-sensitive x-ray fluorescence near total reflection (XFNTR) intensity and fits (lines) plotted over inverse momentum Q_z for graphene oxide films compressed to 20 mN/m and spread on 20 mM CsCl (A) and SrCl$_2$ (B) subphases. Error bars are derived from counting statistics. Sum frequency generation spectroscopy intensity plotted over wavelength for the water region of a graphene oxide film compressed to 20 mN/m and spread over concentrated 20 mM (dark colors) and dilute 0.05 mM (light colors) subphases for CsCl (C) and SrCl$_2$ (D). Typical water band signal is also shown (black). (A colour version of this figure can be viewed online.)
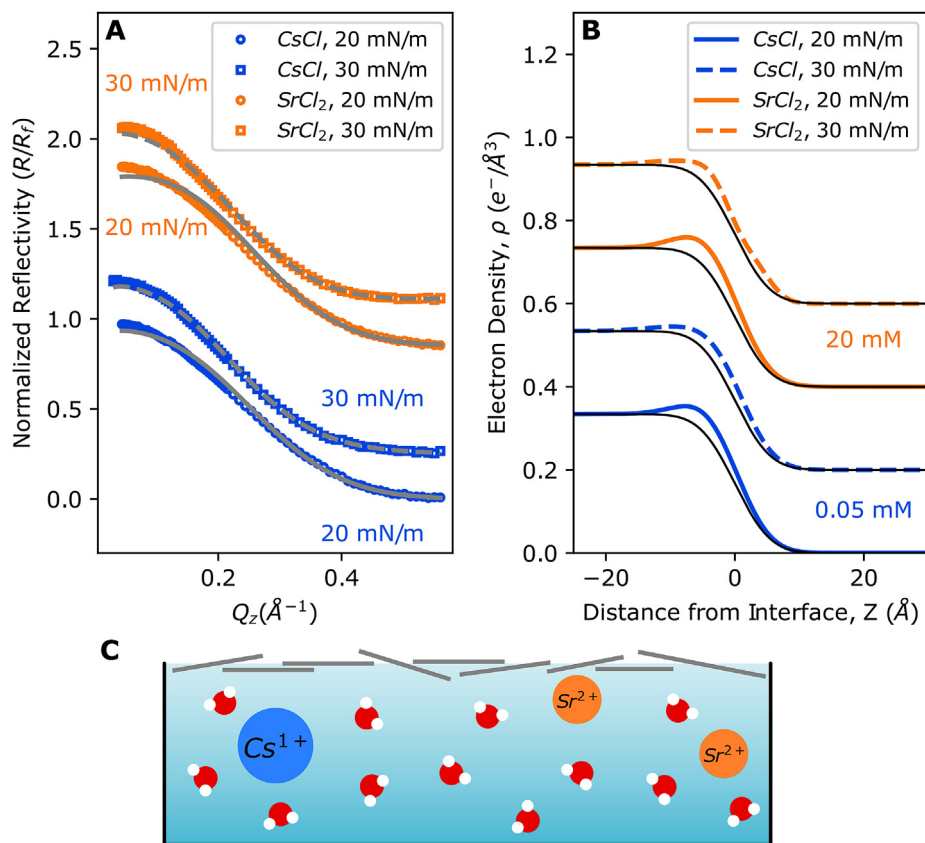
Fig. 6. Normalized x-ray reflectivity plotted over vertical momentum transfer, Q_z, for graphene oxide films compressed to 20 (circles) and 30 (squares) mN/m spread on 0.05 mM CsCl (blue) and 20 mM SrCl$_2$ (orange) subphases (A). Data were fit using a 1 slab models (lines). Data are vertically offset for clarity. Calculated electron density from fitted reflectivity data plotted over distance from interface Z (B) for graphene oxide monolayers compressed to 20 (solid line) and 30 (dashed line) mN/m spread on 0.05 mM YCl$_3$ subphases on 0.05 mM CsCl (blue) and 20 mM SrCl$_2$ (orange) subphases. An ideal interface electron density profile is included (black). Data are vertically offset for clarity. Proposed interfacial structure (not to scale) (C). (A colour version of this figure can be viewed online.)

scattering materials existing in the probed region. Fitting via a 1 slab model provided an electron density of 0.43 e^-/Å^3, a thickness of 7.0 Å, and a roughness of 4.3 Å for 20 mN/m while the 30 mN/m data yielded an electron density of 0.35 e^-/Å^3, a thickness of 15.2 Å, and a roughness of 4.1 Å. Despite the adsorbed Sr^{2+} ions, as confirmed directly with XFNTR and indirectly with SFG, the GO structure does not significantly change compared to the no adsorption case. Again, we speculate the slab in the 20 mN/m system represents a layer of partially hydrated GO, and the slab in the 30 mN/m systems describes a crumpled GO film created from tilted GO flakes. These data support our assertion that Y^{3+} adsorption shows a significant GO structural change. Cs^{1+} and Sr^{2+} ions are likely too facile to significantly adsorb or induce such a rearrangement. These lower valency ions may also be better shielded due to their larger sizes by surrounding anions in solution thus diminishing adsorption capabilities.

4. Conclusions

GO is a promising material for thin film composite membranes and sorbents as it combines the robustness of graphene with chemically active functional groups. Despite the usefulness of GO in these systems, little is known about the molecular-scale details of the metal and water organization near GO films. We present XR, XFNTR, and SFG data considering metal ion adsorption onto interfacial thin GO films. These interface-specific techniques provide the total electron density normal to the interface, the quantitative adsorbed ion density, and information about the hydrogen-

bonding network of water, respectively. Our XFNTR and SFG data shown that trivalent Y^{3+} adsorbs more strongly even in lower concentrations subphases compared to divalent Sr^{2+} and monovalent Cs^{1+} ions. The XR data show a complex GO film structure after Y^{3+} adsorption compared to the no adsorption (0.05 mM CsCl) and minimal ion adsorption (20 mM SrCl^{2+}) cases, as confirmed with both XFNTR and SFG. We posit Y^{3+} can cause the GO flakes to tilt and crumple by attracting the hydrophilic flake edges with its significant charge density. Cs^{1+} and Sr^{2+} are likely too facile to induce such a change and may have reduced effective charges due to local anion shielding. While preferential higher valency ion adsorption is not novel, our detailed x-ray analysis reveals important and substantial changes in the GO film, which can directly impact later application success. These *in situ*, interfacial experiments consider ion interactions with the GO thin film in a relevant aqueous environment, an important improvement over *ex situ* characterization methods.

Additionally, we present for the first time SFG data demonstrating trivalent ion adsorption onto interfacial GO films. Our SFG analysis shows a significant change in the hydrogen-bonding network of interfacial water upon adsorption of Y^{3+} on the GO film, evidenced by the decrease in water region signal. We attribute the observed 3400 cm^{-1} to weakly hydrogen bound water molecules near the GO film or in between the crumpled GO layers. Interestingly, the intensity of this band is nearly independent of subphase concentration, which suggests these water molecules remain unaffected until the total hydrogen-bonding network of water is significantly disrupted. Taken together, these SFG results

imply yttrium ion adsorption is not governed solely by simple electrostatics. Instead, ion adsorption involves a complicated balance between the relevant local surface charge and dehydration energy penalties. Overall, our interfacial-specific techniques provide important molecular information about ion adsorption and supporting future studies of GO for soft-scaffold applications.

CRediT authorship contribution statement

Amanda J. Carr: Conceptualization, Methodology, Formal analysis, Investigation, Data curation, Writing − original draft, Writing − review & editing, Visualization. **Raju Kumal:** Conceptualization, Methodology, Formal analysis, Investigation, Data curation, Writing − review & editing, Visualization. **Wei Bu:** Investigation, Resources. **Ahmet Uysal:** Conceptualization, Methodology, Formal analysis, Supervision, Investigation, Resources, Writing − review & editing, Project administration, Funding acquisition.

Declaration of competing interest

The authors declare that they have no known competing financial interests or personal relationships that could have appeared to influence the work reported in this paper.

Acknowledgment

Appendix A. Supplementary data

Supplementary data to this article can be found online at https://doi.org/10.1016/j.carbon.2022.03.077.

References

[1] G. Liu, W. Jin, N. Xu, Graphene-based membranes, Chem. Soc. Rev. 44 (15) (2015) 5016—5030.
[2] S.J. Rowley-Neale, E.P. Randviir, A.S. Abo Dena, C.E. Banks, An overview of recent applications of reduced graphene oxide as a basis of electroanalytical sensing platforms, Appl. Mater. Today 10 (2018) 218—226.
[3] A. Lerf, H. He, M. Forster, J. Klinowski, Structure of graphite oxide revisited, J. Phys. Chem. B 102 (23) (1998) 4477—4482.
[4] S. Liu, K. Hu, M. Cerruti, F. Barthelat, Ultra-stiff graphene oxide paper prepared by directed-flow vacuum filtration, Carbon 158 (2020) 426—434.
[5] C.J. Bullock, C. Bussy, Biocompatibility considerations in the design of graphene biomedical materials, Adv. Mater. Interfac. 6 (2019) 1900229.
[6] L.J. Cote, F. Kim, J. Huang, Langmuir−Blodgett assembly of graphite oxide single layers, J. Am. Chem. Soc. 131 (3) (2009) 1043—1049.
[7] J. Kim, L.J. Cote, F. Kim, W. Yuan, K.R. Shull, J. Huang, Graphene oxide sheets at interfaces, J. Am. Chem. Soc. 132 (23) (2010) 8180—8186.
[8] D. Lopez-Diaz, M.D. Merchan, M.M. Velazquez, The behavior of graphene oxide trapped at the air water interface, Adv. Colloid Interface Sci. 286 (2020) 102312.
[9] E.F. Sheka, I. Natkaniec, Neutron scattering of parent and reduced graphene oxide, Rev. Adv. Mater. Sci. 49 (2017) 1—27.
[10] B.R. Coleman, T. Knight, V. Gies, Z.J. Jakubek, S. Zou, Manipulation and quantification of graphene oxide flake size: photoluminescence and cytotoxicity, ACS Appl. Mater. Interfaces 9 (34) (2017) 28911—28921.
[11] J. Chen, F. Chi, L. Huang, M. Zhang, B. Yao, Y. Li, C. Li, G. Shi, Synthesis of graphene oxide sheets with controlled sizes from sieved graphite flakes, Carbon 110 (2016) 34—40.
[12] K. Krishnamoorthy, M. Veerapandian, K. Yun, S.J. Kim, The chemical and structural analysis of graphene oxide with different degrees of oxidation, Carbon 53 (2013) 38—49.
[13] H.W. Kim, H.W. Yoon, S.M. Yoon, B.M. Yoo, B.K. Ahn, Y.H. Cho, H.J. Shin, H. Yang, U. Paik, S. Kwon, J.Y. Choi, H.B. Park, Selective gas transport through few-layered graphene and graphene oxide membranes, Science 342 (6154) (2013) 91—95.
[14] R.K. Joshi, P. Carbone, F.C. Wang, V.G. Kravets, Y. Su, I.V. Grigorieva, H.A. Wu, A.K. Geim, R.R. Nair, Precise and ultrafast molecular sieving through graphene oxide membranes, Science 343 (6172) (2014) 752—754.
[15] B. Mi, Graphene oxide membranes for ionic and molecular sieving, Science 343 (6172) (2014) 740—742.
[16] R.R. Nair, H.A. Wu, P.N. Jayaram, I.V. Grigorieva, A.K. Geim, Unimpeded permeation of water through helium-leak-tight graphene-based membranes, Science 335 (6067) (2012) 442—444.
[17] M. Hu, B. Mi, Enabling graphene oxide nanosheets as water separation membranes, Environ. Sci. Technol. 47 (8) (2013) 3715—3723.
[18] G. Romaniak, K. Dybowski, A. Jeziorna, P. Kula, T. Kaźmierczak, Synthesis and characterization of semi-permeable graphene/graphene oxide membranes for water desalination, J. Mater. Sci. 55 (23) (2020) 9775—9786.
[19] P. Sun, M. Zhu, K. Wang, M. Zhong, J. Wei, D. Wu, Z. Xu, H. Zhu, Selective ion penetration of graphene oxide membranes, ACS Nano 7 (1) (2013) 428—437.
[20] R. Liu, G. Arabale, J. Kim, K. Sun, Y. Lee, C. Ryu, C. Lee, Graphene oxide membrane for liquid phase organic molecular separation, Carbon 77 (2014) 933—938.
[21] S. Yang, X. Chen, Z. Zhang, P. Jin, Q. Zhang, X. Wang, The removal of phosphate from aqueous solution through chemical filtration using a sponge filter, Chem. Lett. 47 (1) (2018) 89—91.
[22] M. Hu, S. Zheng, B. Mi, Organic fouling of graphene oxide membranes and its implications for membrane fouling control in engineered osmosis, Environ. Sci. Technol. 50 (2) (2016) 685—693.
[23] A.Y. Romanchuk, A.S. Kuzenkova, A.S. Slesarev, J.M. Tour, S.N. Kalmykov, Cs(I) and Sr(II) sorption onto graphene oxide, Solvent Extr. Ion Exch. 34 (7) (2016) 594—602.
[24] P. Kaewmee, J. Manyam, P. Opaprakasit, G.T. Truc Le, N. Chanlek, P. Sreearunothai, Effective removal of cesium by pristine graphene oxide: performance, characterizations and mechanisms, RSC Adv. 7 (61) (2017) 38747—38756.
[25] A.S. Kuzenkova, A.Y. Romanchuk, A.L. Trigub, K.I. Maslakov, A.V. Egorov, L. Amidani, C. Kittrell, K.O. Kvashnina, J.M. Tour, A.V. Talyzin, S.N. Kalmykov, New insights into the mechanism of graphene oxide and radionuclide interaction, Carbon 158 (2020) 291—302.
[26] M. Xing, S. Zhuang, J. Wang, Adsorptive removal of strontium ions from aqueous solution by graphene oxide, Environ. Sci. Pollut. Res. Int. 26 (29) (2019) 29669—29678.
[27] A.Y. Romanchuk, A.S. Slesarev, S.N. Kalmykov, D.V. Kosynkin, J.M. Tour, Graphene oxide for effective radionuclide removal, Phys. Chem. Chem. Phys. 15 (7) (2013) 2321—2327.
[28] M.T. Nguyen, J. Zhang, V. Prabhakaran, S. Tan, E.T. Baxter, V. Shutthanandan, G.E. Johnson, R. Rousseau, V.A. Glezakou, Graphene oxide as a Pb(II) separation medium: has part of the story been overlooked? JACS Au 1 (6) (2021) 766—776.
[29] Y. Xie, E.M. Helvenston, L.C. Shuller-Nickles, B.A. Powell, Surface complexation modeling of Eu(III) and U(VI) interactions with graphene oxide, Environ. Sci. Technol. 50 (4) (2016) 1821—1827.
[30] B. Hu, Q. Hu, X. Li, H. Pan, X. Tang, C. Chen, C. Huang, Rapid and highly efficient removal of Eu(III) from aqueous solutions using graphene oxide, J. Mol. Liq. 229 (2017) 6—14.
[31] N. Boulanger, A.S. Kuzenkova, A. Iakunkov, A.Y. Romanchuk, A.L. Trigub, A.V. Egorov, S. Bauters, L. Amidani, M. Retegan, K.O. Kvashnina, S.N. Kalmykov, A.V. Talyzin, Enhanced sorption of radionuclides by defect-rich graphene oxide, ACS Appl. Mater. Interfaces 12 (40) (2020) 45122—45135.
[32] Y. Xie, B.A. Powell, Linear free energy relationship for actinide sorption to graphene oxide, ACS Appl. Mater. Interfaces 10 (38) (2018) 32086—32092.
[33] Z.-Q. Bai, Z.-J. Li, C.-Z. Wang, L.-Y. Yuan, Z.-R. Liu, J. Zhang, L.-R. Zheng, Y.-L. Zhao, Z.-F. Chai, W.-Q. Shi, Interactions between Th(iv) and graphene oxide: experimental and density functional theoretical investigations, RSC Adv. 4 (7) (2014) 3340—3347.
[34] H. Mohamud, P. Ivanov, B.C. Russell, P.H. Regan, N.I. Ward, Selective sorption of uranium from aqueous solution by graphene oxide-modified materials, J. Radioanal. Nucl. Chem. 316 (2) (2018) 839—848.
[35] D. Zhao, X. Gao, S. Chen, F. Xie, S. Feng, A. Alsaedi, T. Hayat, C. Chen, Interaction between U(VI) with sulfhydryl groups functionalized graphene oxides investigated by batch and spectroscopic techniques, J. Colloid Interface Sci. 524 (2018) 129—138.
[36] P. Yang, H. Zhang, Q. Liu, J. Liu, R. Chen, J. Yu, J. Hou, X. Bai, J. Wang, Nano-sized architectural design of multi-activity graphene oxide (GO) by chemical post-decoration for efficient uranium(VI) extraction, J. Hazard Mater. 375 (2019) 320—329.
[37] M. Wu, R. Kempaiah, P.J. Huang, V. Maheshwari, J. Liu, Adsorption and

desorption of DNA on graphene oxide studied by fluorescently labeled oligonucleotides, Langmuir 27 (6) (2011) 2731–2738.

[38] K. Chang, Y. Sun, F. Ye, X. Li, G. Sheng, D. Zhao, W. Linghu, H. Li, J. Liu, Macroscopic and molecular study of the sorption and co-sorption of graphene oxide and Eu(III) onto layered double hydroxides, Chem. Eng. J. 325 (2017) 665–671.

[39] P. Mandal, G. Bhattacharya, A. Bhattacharyya, S.S. Roy, S.K. Ghosh, Unravelling the structural changes of phospholipid membranes in presence of graphene oxide, Appl. Surf. Sci. (2021) 539.

[40] V.N. Bliznyuk, N.A. Conroy, Y. Xie, R. Podila, A.M. Rao, B.A. Powell, Increase in the reduction potential of uranyl upon interaction with graphene oxide surfaces, Phys. Chem. Chem. Phys. 20 (3) (2018) 1752–1760.

[41] D. Barker, A. Fors, E. Lindgren, A. Olesund, E. Schroder, Filter function of graphene oxide: trapping perfluorinated molecules, J. Chem. Phys. 152 (2) (2020), 024704.

[42] F. Li, J. Zhao, Z. Chen, Fe-anchored graphene oxide: a low-cost and easily accessible catalyst for low-temperature CO oxidation, J. Phys. Chem. C 116 (3) (2012) 2507–2514.

[43] W. Peng, H. Li, Y. Liu, S. Song, A review on heavy metal ions adsorption from water by graphene oxide and its composites, J. Mol. Liq. 230 (2017) 496–504.

[44] D.S. Sutar, P.K. Narayanam, G. Singh, V.D. Botcha, S.S. Talwar, R.S. Srinivasa, S.S. Major, Spectroscopic studies of large sheets of graphene oxide and reduced graphene oxide monolayers prepared by Langmuir–Blodgett technique, Thin Solid Films 520 (18) (2012) 5991–5996.

[45] L.J. Cote, F. Kim, J. Huang, Langmuir-Blodgett assembly of graphite oxide single layers, J. Am. Chem. Soc. 131 (3) (2009) 1043–1049.

[46] K. Bramhaiah, N.S. John, Facile synthesis of reduced graphene oxide films at the air–water interface and in situ loading of noble metal nanoparticles, Adv. Nat. Sci. Nanosci. Nanotechnol. 3 (4) (2012).

[47] R.S. Hidalgo, D. Lopez-Diaz, M.M. Velazquez, Graphene oxide thin films: influence of chemical structure and deposition methodology, Langmuir 31 (9) (2015) 2697–2705.

[48] G.A. Turpin, S.A. Holt, J.M.P. Scofield, B.M. Teo, R.F. Tabor, Spontaneous adsorption of graphene oxide to oil–water and air–water interfaces by adsorption of hydrotropes, Adv. Mater. Interfac. 7 (9) (2020).

[49] S. Fang, T. Chen, B. Chen, Y. Xiong, Y. Zhu, M. Duan, Graphene oxide at oil-water interfaces: adsorption, assembly & demulsification, Colloids Surf., A 511 (2016) 47–54.

[50] N. Bonatout, F. Muller, P. Fontaine, I. Gascon, O. Konovalov, M. Goldmann, How exfoliated graphene oxide nanosheets organize at the water interface: evidence for a spontaneous bilayer self-assembly, Nanoscale 9 (34) (2017) 12543–12548.

[51] R. David, A. Tuladhar, L. Zhang, C. Arges, R. Kumar, Effect of oxidation level on the interfacial water at the graphene oxide-water interface: from spectroscopic signatures to hydrogen-bonding environment, J. Phys. Chem. B 124 (37) (2020) 8167–8178.

[52] T. Ishiyama, T. Imamura, A. Morita, Theoretical studies of structures and vibrational sum frequency generation spectra at aqueous interfaces, Chem. Rev. 114 (2014) 8447–8470.

[53] F.M. Geiger, Second harmonic generation, sum frequency generation, and χ(3): dissecting environmental interfaces with a nonlinear optical Swiss Army knife, Annu. Rev. Phys. Chem. 60 (2009) 61–83.

[54] Z. Zhang, J. Kim, R. Khoury, M. Saghayezhian, L.H. Haber, E. Plummer, Surface sum frequency generation spectroscopy on non-centrosymmetric crystal GaAs (001), Surf. Sci. 664 (2017) 21–28.

[55] R. David, R. Kumar, Reactive events at the graphene oxide-water interface, Chem. Commun. 57 (88) (2021) 11697–11700.

[56] K. Lovering, S. Nayak, W. Bu, A. Uysal, The role of specific ion effects in ion transport: the case of nitrate and thiocyanate, J. Phys. Chem. C 124 (2019) 573–581.

[57] W. Rock, B. Qiao, T. Zhou, A.E. Clark, A. Uysal, Heavy anionic complex creates a unique water structure at a soft charged interface, J. Phys. Chem. C 122 (2018) 29228–29236.

[58] S. Nayak, R.R. Kumal, Z. Liu, B. Qiao, A. Clark, A. Uysal, Origins of clustering of metalate-extractant complexes in liquid-liquid extraction, ACS Appl. Mater. Interfaces 13 (2021) 24194–24206.

[59] R. Kumal, S. Nayak, W. Bu, A. Uysal, Chemical potential driven reorganization of anions between stern and diffuse layers at the air/water interface, J. Phys. Chem. C 126 (2) (2022) 1140–1151.

[60] P.E. Ohno, H.-f. Wang, F.M. Geiger, Second-order spectral lineshapes from charged interfaces, Nat. Commun. 8 (2017) 1–9.

[61] Y.-C. Wen, S. Zha, X. Liu, S. Yang, P. Guo, G. Shi, H. Fang, Y.R. Shen, C. Tian, Unveiling microscopic structures of charged water interfaces by surface-specific vibrational spectroscopy, Phys. Rev. Lett. 116 (2016) 16101–16105.

[62] R.R. Kumal, T.E. Karam, L.H. Haber, Determination of the surface charge density of colloidal gold nanoparticles using second harmonic generation, J. Phys. Chem. C 119 (2015) 16200–16207.

[63] M.K. Bera, W. Bu, A. Uysal, Liquid surface x-ray scattering, in: J. Faust, J. House (Eds.), Physical Chemistry of Gas-Liquid Interfaces, Elsevier, 2018, pp. 167–194.

[64] S.M. Danauskas, D. Li, M. Meron, B. Lin, K.Y.C. Lee, Stochastic fitting of specular X-ray reflectivity data using StochFit, J. Appl. Crystallogr. 41 (6) (2008) 1187–1193.

[65] A. Thompson, D. Attwood, E. Gullikson, M. Howells, K.-J. Kim, J. Kirz, J. Kortright, I. Lindau, Y. Lu, P. Pianetta, A. Robinson, J. Scofield, J. Underwood, G. Williams, H. Winick, X-ray Data Booklet, 3 ed., Lawrence Berkeley National Lab, Berkeley, CA, 2009.

[66] W. Bu, M. Mihaylov, D. Amoanu, B. Lin, M. Meron, I. Kuzmenko, L. Soderholm, M.L. Schlossman, X-ray studies of interfacial strontium–extractant complexes in a model solvent extraction system, J. Phys. Chem. B 118 (43) (2014) 12486–12500.

[67] S. Nayak, K. Lovering, W. Bu, A. Uysal, Anions enhance rare earth adsorption at negatively charged surfaces, J. Phys. Chem. Lett. 11 (11) (2020) 4436–4442.

[68] A. Uysal, W. Rock, B. Qiao, W. Bu, B. Lin, Two-step adsorption of PtCl6 2− complexes at a charged Langmuir monolayer: role of hydration and ion correlations, J. Phys. Chem. C 121 (45) (2017) 25377–25383.

[69] A.J. Carr, S.S. Lee, A. Uysal, Trivalent ion overcharging on electrified graphene, J. Phys. Condens. Matter 34 (2022), 144001.

[70] A. Tuladhar, S.M. Piontek, L. Frazer, E. Borguet, Effect of halide anions on the structure and dynamics of water next to an alumina (0001) surface, J. Phys. Chem. C 122 (24) (2018) 12819–12830.

[71] K.C. Jena, P.A. Covert, D.K. Hore, The effect of salt on the water structure at a charged solid surface: differentiating second- and third-order nonlinear contributions, J. Phys. Chem. Lett. 2 (9) (2011) 1056–1061.

[72] G. Ma, X. Chen, H.C. Allen, Dangling OD confined in a Langmuir monolayer, J. Am. Chem. Soc. 129 (45) (2007) 14053–14057.

[73] S. Eigler, C. Dotzer, F. Hof, W. Bauer, A. Hirsch, Sulfur species in graphene oxide, Chem. Eur J. 19 (29) (2013) 9490–9496.

[74] W. Sung, W. Wang, J. Lee, D. Vaknin, D. Kim, Specificity and variation of length scale over which monovalent halide ions neutralize a charged interface, J. Phys. Chem. C 119 (13) (2015) 7130–7137.

[75] A. Sthoer, E.M. Adams, S. Sengupta, R.W. Corkery, H.C. Allen, E.C. Tyrode, La3+ and Y3+ interactions with the carboxylic acid moiety at the liquid/vapor interface: identification of binding complexes, charge reversal, and detection limits, J. Colloid Interface Sci. 608 (2022) 2169–2180.

[76] Y. Hong, J. He, C. Zhang, X. Wang, Probing the structure of water at the interface with graphene oxide using sum frequency generation vibrational spectroscopy, J. Phys. Chem. C 126 (3) (2022) 1471–1480.

[77] A. Uysal, M. Chu, B. Stripe, A. Timalsina, S. Chattopadhyay, C.M. Schlepütz, T.J. Marks, P. Dutta, What x rays can tell us about the interfacial profile of water near hydrophobic surfaces, Phys. Rev. B 88 (3) (2013), 035431.

[78] P. Sun, E.A. Binter, Z. Liang, M.A. Brown, A.V. Gelis, I. Benjamin, M.K. Bera, B. Lin, W. Bu, M.L. Schlossman, Antagonistic role of aqueous complexation in the solvent extraction and separation of rare earth ions, ACS Cent. Sci. 7 (11) (2021) 1908–1918.